

# Ubiquitous evaluation of layer potentials using Quadrature by Kernel-Independent Expansion

Abtin Rahimian · Alex Barnett · Denis Zorin

**Abstract** We introduce a quadrature scheme — QBKIX — for the high-order accurate evaluation of layer potentials associated with general elliptic PDEs near to and on the domain boundary. Relying solely on point evaluations of the underlying kernel, our scheme is essentially PDE-independent; in particular, no analytic expansion nor addition theorem is required. Moreover, it applies to boundary integrals with singular, weakly singular, and hypersingular kernels.

Our work builds upon Quadrature by Expansion (QBX), which approximates the potential by an analytic expansion in the neighborhood of each expansion center. In contrast, we use a sum of fundamental solutions lying on a ring enclosing the neighborhood, and solve a small dense linear system for their coefficients to match the potential on a smaller concentric ring.

We test the new method with Laplace, Helmholtz, Yukawa, Stokes, and Navier (elastostatic) kernels in two dimensions (2D) using adaptive, panel-based boundary quadratures on smooth and corner domains. Advantages of the algorithm include its relative simplicity of implementation, immediate extension to new kernels, dimension-independence (allowing simple generalization to 3D), and compatibility with fast algorithms such as the kernel-independent FMM.

## 1 Introduction

The boundary integral method is a powerful tool for solving linear partial differential equations (PDEs) of classical physics with piecewise constant material coefficients, with applications including electromagnetic scattering, molecular electrostatics, viscous fluid flow, and acoustics. It involves exploiting Green’s theorems to express the solution in terms of an unknown “density” function defined on the domain boundaries or material interfaces, using the physical boundary condition to formulate an integral equation for this density, and finally obtaining a linear algebraic system via Galerkin, Nyström, or other discretization. Compared to commonly used differential formulations, boundary integral methods have a number of advantages: decreasing the dimension of the problem that needs to be discretized, avoiding meshing the volume, and improving conditioning. For instance, the integral equation can often be chosen to be a Fredholm equation of the second kind, resulting in a well-conditioned linear system which can be solved by a Krylov subspace methods in a few iterations. All these considerations are particularly important for problems with complicated and moving geometries [27, 45, 15, 41].

The main difficulty in using boundary integral methods is the need to evaluate singular and nearly-singular integrals: (i) Evaluating system matrix entries requires evaluation of the potential on the sur-

---

Abtin Rahimian · Denis Zorin

Courant Institute of Mathematical Sciences, New York University, New York, NY 10003 E-mail: arahimian@acm.org, E-mail: dzorin@cims.nyu.edu

Alex Barnett

Department of Mathematics, Dartmouth College, Hanover, NH 03755 E-mail: ahb@math.dartmouth.edu

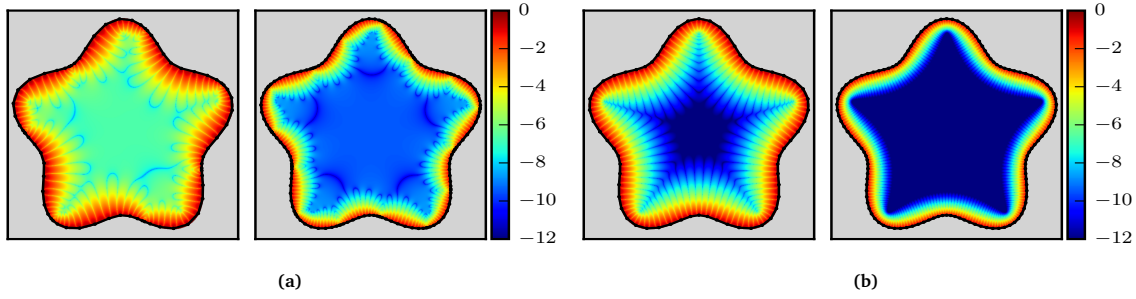


**Fig. 1.1:** Evaluation error plotted in the solution domain due to approximating the Laplace double-layer potential Eq. (1.1) using a quadrature designed for smooth functions. Logarithm of absolute error;  $\log_{10} |\tilde{u}(\mathbf{x}) - u(\mathbf{x})|$ , where  $u$  is the true solution and  $\tilde{u}$  is the discrete approximation using smooth quadrature is plotted for the case of constant density  $\phi \equiv 1$ . (a) shows composite quadrature with  $M = 7$  (left) or  $M = 15$  (right) panels each with  $q = 10$  Gauss-Legendre nodes. (b) shows the global composite trapezoid rule with  $N = 64$  (left) or  $N = 128$  (right) nodes.

face, which involves a *singular* integral; (ii) Once the density is solved for, the desired solution must still be evaluated in the form of a potential. As an evaluation point approaches the boundary of the domain, the peak in the resulting integrand becomes taller and narrower, giving rise to what is referred to as a *near-singular* integral. The result is an arbitrarily high loss of accuracy, if the distance from points to the surface is not bounded from below, when a quadrature scheme designed for smooth integrands is used [2, Section 7.2.1] and [3].

Figure 1.1 illustrates the near-singular evaluation of the solution  $u$  of the Dirichlet Laplace equation in a simple smooth domain, which is represented by the double-layer potential

$$u(\mathbf{x}) = \frac{1}{2\pi} \int_{\Gamma} \frac{\partial}{\partial \mathbf{n}_y} \log \frac{1}{\|\mathbf{x} - \mathbf{y}\|} \cdot \phi(\mathbf{y}) ds(\mathbf{y}), \quad (1.1)$$

where  $\phi$  is the density defined on the boundary  $\Gamma$ . The growth in error as  $\mathbf{x}$  approaches  $\Gamma$  is apparent in all four plots (showing panel-based and global quadratures with different numbers of nodes  $N$ ). Although the width of the high-error layer near the boundary shrinks like  $1/N$  [3], the error always reaches  $\mathcal{O}(1)$  at the boundary. The goal of this paper is to present a flexible scheme that handles both tasks (singular and near-singular evaluation) to high-order accuracy in a kernel-independent (i.e., PDE-independent) manner.

**Related work.** Designing quadrature schemes for singular and near-singular integrals has a long and rich history [2, 38]. Until recently, the quadrature methods were designed specifically for either on-surface evaluation or near-surface evaluation. Many of the on-surface integration quadrature are specific to a certain type of kernel (singularity), e.g.,  $\log|\mathbf{r}|$  in 2D or  $1/|\mathbf{r}|$  in 3D [31, 1, 25, 35, 37, 47, 48, 53, 10]; the former case is reviewed in [24].

A popular method for on-surface quadrature is the product integration (in 2D, for the global trapezoid rule see [2, Section 4.2] or [38, Section 12.3], and for panel-based rules see [27]). In this context, an analytic convolution of the kernel with each function in some basis set is found, reducing evaluation of the integral to projection of the boundary density onto that basis set.

Another approach for on-surface evaluation is singularity subtraction, where the integrand is modified by subtracting an expression that eliminates its singularity [16, Chapter 2] and [42, 29]. However, this leaves high-order singularities in the kernel which makes the higher derivatives of the kernels unbounded, limiting the accuracy of the quadrature scheme. Alternatively, for weakly singular kernels, one can use transformations to cancel the singularity by the decay of area element (e.g., in 3D using Duffy transformation [17] or polar coordinates) [13, 21, 33, 46, 54, 19, 30, 52, 20, 22]. To achieve a high convergence order, these methods need some form of partition of unity so that a high-order polar patch can be constructed around each point [54].

One can also regularize the kernel and then exploit quadrature schemes for smooth functions [39, 50]. However, to achieve higher accuracy, the effect of regularization needs to be corrected by using analytic expressions (e.g., asymptotic analysis) for the integrand [6]. Finally, there exist special high-order quadrature schemes for domains with corners, either via reparametrization [36, 38], panel-wise geometric refinement [26], or by custom generalized Gaussian quadratures [11, 12].

We now turn to near-singular integrals (evaluation close to the surface), which has traditionally been handled as a distinct task [27, 5, 6, 23, 33, 49, 26]. Beale and coauthors [55, 7, 49] use regularization methods to remove the singularity of the integral. To correct the error introduced by the regularization, they perform asymptotic analysis and find correction expressions. Some authors used singularity cancellation (e.g., using local polar coordinates) in evaluating near-singular integrals [23, 33]. Interpolation along carefully-chosen lines connecting distant points (where a smooth quadrature is accurate) to an on-surface point has also been successful [54, 43].

Recently, unified approaches to on-surface and close evaluation have been proposed, the first being the 2D Laplace high-order global and panel-based quadratures of Helsing and Ojala [27]. This approach has been extended to near-singular Stokes single- and double-layer kernels with global [5] and panel-based [41] quadrature. The use of *local expansions* — analytic separation of variables to the PDE solutions analogous to a Taylor series in the complex plane — for the evaluation of integrals near the boundary was introduced in [3].

In this scheme, a refined smooth quadrature is needed to accurately evaluate the expansion coefficients via the addition theorem. It was observed that the expansion can also be used to evaluate at target points on the boundary of the domain, if certain conditions are satisfied [18]; this was used to construct a unified quadrature scheme — Quadrature by Expansion (QBX) — for near and on-surface evaluation of integrals [34]. Racch [44] recently showed how to efficiently combine QBX evaluations with the fast multipole method.

However, powerful as they are, QBX schemes require both a local expansion and addition theorem particular to each PDE, which would be algebraically tedious especially for vector-valued PDEs such as Stokes and elastostatics. This motivates the need for a scheme that can handle multiple PDEs without code changes. The present work fills this gap.

**Overview and model problems.** As with QBX, we construct an approximate representation for PDE solutions in a small region abutting the boundary, then use it for near and on-surface evaluations. However, in contrast to QBX, our representation is an *equivalent density* on a closed curve enclosing this region; when discretized, this gives a ring of “proxy” point sources (also known as the *method of fundamental solutions* [8]). Matching is done at a second smaller ring of “check” points where a refined smooth quadrature is accurate, thus the only dependence on the PDE is via point-to-point kernel evaluations — the method is kernel-independent, and essentially PDE-independent.

We focus on Dirichlet boundary-value problems

$$\mathcal{L}u = 0 \quad \text{in } \Omega, \quad (1.2)$$

$$u = f \quad \text{on } \Gamma, \quad (1.3)$$

where  $\Omega$  is a simply-connected interior domain with smooth boundary  $\Gamma$ , for the following partial differential operators:

$$\mathcal{L}u = \begin{cases} \Delta u & \text{Laplace,} \\ (\Delta - \lambda^2)u & \text{Yukawa,} \\ (\Delta + \omega^2)u & \text{Helmholtz } (\text{Im } \omega \geq 0), \\ \Delta u - \nabla p & \text{Stokes (subject to } \nabla \cdot u = 0), \\ \Delta u + \frac{1}{1-2\nu} \nabla \nabla \cdot u & \text{Elastostatic.} \end{cases} \quad (1.4)$$

To obtain well-conditioned formulations of the problem, we represent the solution of Eqs. (1.2–1.4) for  $\mathbf{x} \in \Omega$  by the double-layer potentials

$$u(\mathbf{x}) = \mathcal{D}[\phi](\mathbf{x}) := \int_{\Gamma} \frac{\partial \Phi(\mathbf{x}, \mathbf{y})}{\partial \mathbf{n}_y} \phi(\mathbf{y}) \, ds(\mathbf{y}), \quad (1.5)$$

where  $\Phi$  is the fundamental solution for the operator  $\mathcal{L}$ , and  $\phi$  is an unknown density. The fundamental solutions for the operators listed in Eq. (1.4) are given in Appendix A. A standard step (see, e.g., [28]) is now to substitute Eq. (1.5) into the boundary condition and use the jump relation for the potential to obtain the second-kind integral equation

$$-\frac{1}{2}\phi(\mathbf{x}) + (D\phi)(\mathbf{x}) = f(\mathbf{x}), \quad \text{for } \mathbf{x} \in \Gamma, \quad (1.6)$$

where  $D$  is the restriction of  $\mathcal{D}$  to the curve. Here, the integral implicit in the integral operator  $D$  must be taken in the principal value sense.

**Discretization and overall approach.** In general, a smooth quadrature is a set of nodes  $\mathbf{x}_i \in \Gamma$  with associated weights  $w_i$ , such that

$$\int_{\Gamma} f \, ds \approx \sum_{i=1}^N w_i f(\mathbf{x}_i), \quad (1.7)$$

holds to high accuracy for smooth functions on  $\Gamma$ —including the density  $\phi$ . In this work, we use  $q$ -node Gauss–Legendre quadrature scheme on panels, and for convergence tests, we increase the number of panels while holding  $q$  fixed. Upon discretization, Eq. (1.6) will be approximated by the linear system

$$\sum_{j=1}^N A_{ij} \phi_j = f(\mathbf{x}_i), \quad i = 1, \dots, N, \quad (1.8)$$

whose solution  $\boldsymbol{\phi} = \{\phi_j\}_{j=1}^N$  approximates the density values at the collocation points. In practice, for large problems, the matrix  $A$  is not constructed explicitly, but instead the matrix-vector product  $A\boldsymbol{\phi}$  is evaluated using the fast multipole method. We test the QBKIX scheme both for applying matrix  $A$  (i.e., on-surface evaluation) and evaluating the solution at arbitrary points, near-evaluation in particular.

The system matrix elements are computed using the Nyström method [38, Ch. 12]. If the operator  $D$  is smooth on  $\Gamma \times \Gamma$ , we use a smooth Nyström formula; e.g., for Laplace,

$$A_{ij} = \begin{cases} \frac{\partial \Phi(\mathbf{x}_i, \mathbf{x}_j)}{\partial \mathbf{n}_{\mathbf{x}_j}} w_j, & i \neq j, \\ -\frac{1}{2} - \frac{\kappa(\mathbf{x}_j)}{4\pi} w_j, & i = j, \end{cases} \quad (1.9)$$

where  $\kappa(\mathbf{x})$  is the curvature at  $\mathbf{x} \in \Gamma$ . This discretization achieves super-algebraic convergence. However, for Yukawa and Helmholtz in 2D, and all 3D elliptic kernels, singular quadrature is needed.

In contrast to established approaches using specialized singular quadratures, we follow the idea underlying the QBX method: *applying  $A$  to a vector  $\boldsymbol{\phi}$  is equivalent to evaluating the interior limit of the double-layer potential due to a smooth density interpolated from  $\boldsymbol{\phi}$ .* This observation leads to the QBKIX idea: use a fast algorithm combined with the smooth quadrature scheme, Eq. (1.7), for point evaluation away from the surface—at points we refer to as *check points*—and interpolate from these points to the on surface point, to compute  $A\boldsymbol{\phi}$  for the Krylov iteration. As this interpolation can be done using points on one or both sides of the surface, in Section 4.2 we compare “one-sided” and “two-sided” variants of QBKIX with respect to their spectra and iterative convergence rates.

Although we are focusing on interior Dirichlet tests and Nyström-style sampled representation of the density in this work, QBKIX is applicable for Neumann or other boundary conditions, and Galerkin and other discretization types. Moreover, while the approach presented in this paper is restricted to 2D, there is no fundamental obstacle to an extension to 3D.

The rest of the paper is structured as follows. In Section 2 we present the QBKIX algorithm for integration. We present an error analysis in Section 3. In Section 4, and report the results of numerical experiments quantifying the accuracy of the method for a number of representative problems.

## 2 Algorithms

Given a closed curve  $\Gamma \subset \mathbb{R}^2$  with interior  $\Omega$ , and Dirichlet data  $f$  on  $\Gamma$ , our goal is to numerically solve the integral equation (1.6) for density and evaluate the solution of the underlying PDE at an arbitrary target point  $\mathbf{x} \in \overline{\Omega}$ . We assume that  $\Gamma$  is parametrized by a  $2\pi$ -periodic piecewise-smooth function  $\mathbf{X}(t)$ , so that the arc length element is  $ds = |\mathbf{X}'(t)| dt$ ,  $|\mathbf{X}'(t)|$  is bounded from below, and that  $\mathbf{X}(t)$  and the data function  $f(t)$  may be evaluated at any  $t \in [0, 2\pi)$ . The boundary is subdivided into *panels*, which can be of different lengths, on which the native quadrature rule is defined (we use Gauss–Legendre quadrature), at  $q$  nodes  $\mathbf{x}_j$  per panel. We assume that the density is available as a vector of samples  $\phi(\mathbf{x}_j)$  at the quadrature nodes.

### 2.1 Single-point evaluation

We describe our method in the simplest form for computing the solution accurately at a given point  $\mathbf{x}$ . We assume that there is a single point on  $\Gamma$  closest to  $\mathbf{x}$ , on a panel of length  $L$ . We assume that at a distance  $2\delta$  along the normal to the panel at any point, the native quadrature meets the target accuracy of evaluation, so the distance from  $\mathbf{x}$  to the surface is less than  $2\delta$ . We discuss how  $\delta$  is chosen and how to ensure that this condition holds after the algorithm formulation.

The local geometric configuration of various types of points we are using in our algorithm is shown in Figure 2.2. The setup shown in the image is for computing the potential accurately for any point  $\mathbf{x}$  inside a disk  $B_\delta^c$  of radius  $\delta$  centered at  $\mathbf{c}$ , touching the surface at a point  $\mathbf{x}_0$  on a panel of length  $L$ .

The points we use in the algorithm are placed on two concentric circles with the same center as the evaluation disk  $B_\delta^c$ . The *proxy points* on a circle  $\partial B_R^c$  of a radius  $R > \delta$ , where we compute *equivalent density* values, are used to approximate the solution inside  $B_\delta^c$ . The *check points*  $\mathbf{z}_i$  are on a circle  $\partial B_{r_c}^c$  of a radius  $r_c < \delta$ . At these points, we evaluate the solution accurately by using a smooth quadrature on panels refined by a factor  $\beta$ . The check points are used to compute the equivalent density values at the proxy points as described below.

The algorithm depends on a number of parameters; these parameters need to be chosen appropriately to achieve an overall target accuracy. Specific choices are discussed in the next section. The key steps in the algorithm are

- (1) **Set-up of proxy and check points.** We choose a center  $\mathbf{c} \in \Omega$  at a distance  $\delta$  from  $\Gamma$ , such that  $\mathbf{x}$  is no further from  $\mathbf{c}$  than  $\delta$ . E.g., for  $\mathbf{x} \in \Gamma$ , we set  $\mathbf{c} = \mathbf{x} - \delta \mathbf{n}$ , where  $\mathbf{n}$  is the outward normal.  $n_p$  proxy points  $\mathbf{y}_j$  are arranged equally on the circle of radius  $R$  with center  $\mathbf{c}$ , where  $R > \delta$  is of order  $L$ . Similarly  $n_c$  check points  $\mathbf{z}_i$  are arranged on the concentric circle of radius  $r_c < \delta$  (Fig. 2.1).
- (2) **Upsampling the density.** Each panel is split into  $\beta$  panels corresponding to equal ranges of  $t$ , to give a set of  $\beta N$  fine-scale nodes  $\tilde{\mathbf{x}}_l$  with weights  $\tilde{w}_l$ . The global factor  $\beta$  is chosen so that the solution can be evaluated accurately at the check points, i.e., at a distance  $\delta - r_c$  from the surface. The density is interpolated from its original samples  $\phi(\mathbf{x}_j)$  on each panel, using  $q^{\text{th}}$  order Lagrange interpolation to the fine-scale nodes, to give the refined vector of samples  $\tilde{\phi}_l$ ,  $l = 1, \dots, \beta N$ .

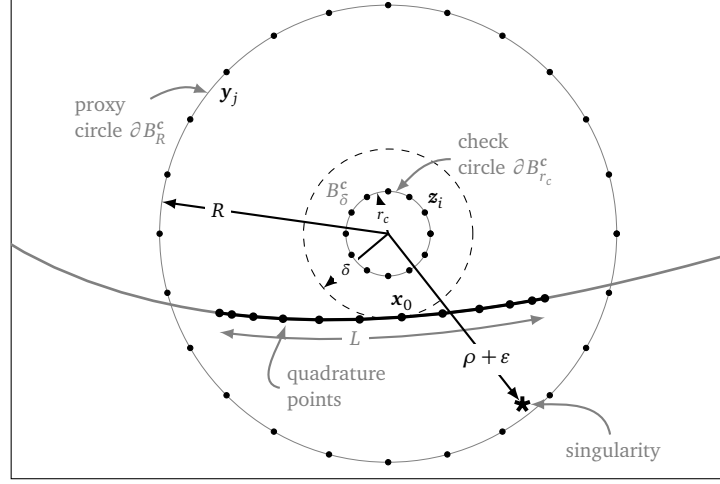


**Fig. 2.1:** SCHEMATIC OF A KERNEL-INDEPENDENT EXPANSION. Geometry of QBKIX, with proxy and check circles centered at  $c$  near a panel of length  $L$  of the boundary  $\Gamma$  discretized with  $q$  Gauss-Legendre sample points. The evaluation domain  $B_\delta^c$  is a disc centered at  $c$  of radius  $\delta$  (dashed circle abutting the boundary at  $x_0$ ). The points  $z_i$  are the check points on the circle  $\partial B_{r_c}^c$  of radius  $r_c$ , and  $y_j$  are the proxy points on the circle  $\partial B_R^c$  of radius  $R$ . For error analysis, the singularities of the exact solution are assumed to be at a distance farther than  $\rho$  from  $c$ . Note that, for clarity, the relative sizes of circles and distances between samples are different from the ones actually used.

- (3) **Direct upsampled evaluation at check points.** The integral is evaluated at each check point  $z_i$  using the fine-scale boundary native quadrature:

$$\tilde{u}(z_i) = \sum_{l=1}^{\beta N} \frac{\partial \Phi(z_i, x_l)}{\partial \mathbf{n}_{x_l}} \tilde{\phi}_l \tilde{w}_l. \quad (2.1)$$

Denote by  $\tilde{\mathbf{u}} := \{\tilde{u}(z_i)\}_{i=1}^{n_c}$  the column vector of these values at the check points.

- (4) **Solving for the equivalent density values.** Next, we construct an  $n_c \times n_p$  matrix  $Q$  with elements

$$Q_{ij} = \Phi(z_i, y_j). \quad (2.2)$$

Applying  $Q$  to a vector of density values at proxy points computes a periodic trapezoidal rule approximation to the single-layer potential corresponding to this density evaluated at check points. Then we solve a small, dense, and ill-conditioned linear system

$$Q\alpha = \tilde{\mathbf{u}}, \quad (2.3)$$

in the least-squares sense, to get the set of proxy density values  $\alpha := \{\alpha_j\}_{j=1}^{n_p}$ . The ill-conditioning arises from the exponential decay of singular values in the single-layer operator between concentric circles (see Fig. 3.1). Despite this, if Eq. (2.3) is solved in a backward-stable manner, a high-accuracy result is obtained (cf. [4], we explain the details below for completeness).

- (5) **Evaluation of the proxy sources at the target.** Finally, the equivalent density is evaluated at the target  $x$ ,

$$\hat{u}(x) = \sum_{j=1}^{n_p} \alpha_j \Phi(x, y_j), \quad (2.4)$$

We may view this as an approximation for the true solution  $u$  in the basis of fundamental solutions centered at the proxy points, that holds to high accuracy in the disk  $B_\delta^c$ .

Figure 2.2 illustrates the stages of QBKIX evaluation for a set of target points lying in a single disk  $B_\delta^c$ . The final evaluation of Eq. (2.4) over the disc of target points has around 12 digits of accuracy.

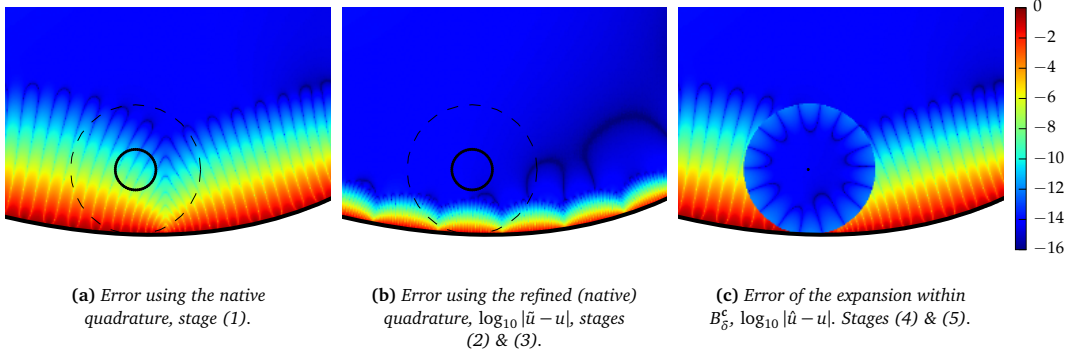


**Fig. 2.2:** STAGES OF QBKIX CONSTRUCTION. The stages given in Section 2 are illustrated using plots of the  $\log_{10}$  of the evaluation error near the boundary, for the double-layer density  $\phi \equiv 1$  for Laplace's equation. The evaluation disc  $B_\delta^c$  (dashed circle), check circle  $\partial B_{r_c}^c$  (solid circle) are shown, and proxy points are not shown.

**Handling the ill-conditioned linear solves.** The ill-conditioned system Eq. (2.3) is solved by applying a regularized pseudo-inverse, as follows. Let  $\varepsilon_{\text{pinv}}$  be the desired relative accuracy for inversion; typically we set  $\varepsilon_{\text{pinv}} = 10^{-14}$ . Then, taking the singular value decomposition (SVD) [51]  $Q = U\Sigma V^*$  with  $\Sigma = \text{diag}\{\sigma_j\}$  being the diagonal matrix of singular values, we write  $\Sigma^\dagger := \text{diag}\{\sigma_j^\dagger\}$  where

$$\sigma_j^\dagger = \begin{cases} \sigma_j^{-1}, & \sigma_j > \varepsilon_{\text{pinv}} \sigma_1, \\ 0, & \text{otherwise.} \end{cases} \quad (2.5)$$

Then we use the solution

$$\alpha := V(\Sigma^\dagger U^* u). \quad (2.6)$$

Note that the matrices  $U^*$  and  $V$  must be applied in two separate steps (as indicated by the parenthesis) for backward stability [51], since a matrix-vector multiply with the single pseudo-inverse matrix  $Q^\dagger := V\Sigma^\dagger U^*$  is unstable due to round-off error caused by its large entries. If  $k$  is the number of singular values greater than  $\varepsilon_{\text{pinv}}$ , i.e., the numerical  $\varepsilon_{\text{pinv}}$ -rank of the matrix  $Q$ , the factors  $V$  and  $U^*$  have sizes  $n_p \times k$  and  $k \times n_c$  respectively.

**Parameter summary.** The algorithm described above uses a number of parameters, which we summarize here.

The following parameters are defined globally:

- The quadrature order  $q$ , which determines the number of samples per panel, and both far-field evaluation accuracy and, together with  $\beta$ , the accuracy of evaluation at check points. This parameter is selected arbitrarily based on the desired overall accuracy. We use  $q = 16$ , which is sufficient for full double precision of integration in the far field.
- The panel refinement factor  $\beta$  which needs to be chosen to maintain desired accuracy for check point evaluation.
- The numbers of proxy points  $n_p$  and check points  $n_c$ ; the former determines how accurate the approximation inside  $B_\delta^c$  can be and the latter is chosen to have enough sampling.

Three additional parameters, the accurate evaluation distance  $\delta$ , the proxy point circle radius  $R$  and the check point circle radius  $r_c$ , are panel-dependent, and are chosen with respect to panel size  $L$ . A careful choice of all of these, as fractions of  $L$ , is needed to achieve a target error without requiring excessive refinement. We discuss the choice of these parameters in Section 3.



**Defining panels.** In our experiments, we consider two ways of defining panels. The first approach is primarily needed to understand the convergence of the method with respect to the number of panels, i.e., for a given number of panels, we determine the error. In this case, we simply partition the parametric domain of  $X(t)$  into  $M$  equal-sized intervals, with one panel corresponding to each interval. We assume the parametrization to be sufficiently close to an arclength parametrization, so that the panel length has little variation, and choose  $M$  to be fine enough so that the geometric condition on the check points is satisfied.

In a more practical scenario, when a target error is specified, we need to determine panel sizes adaptively. The key requirement that needs to be satisfied by panels is that the accuracy of check-point evaluation at stage 2 matches the target accuracy in the far field (i.e., points farther than  $2\delta$  from the boundary). The adaptive refinement starts with one panel covering the entire boundary, then recursively splitting panels into two equal pieces in parameter  $t$ , until all panels are deemed *admissible* or their length is less than a set tolerance  $\varepsilon$ .

A panel is admissible if (i) the interpolation of  $X(t)$  and  $f(t)$  from a  $q$ -node panel at the collocation points of the two  $q$ -nodes Gauss–Legendre panels (obtained by splitting the coarse panel to two pieces) matches the direct evaluation of  $X$  and  $f$  on the finer nodes, to a maximum absolute tolerance  $\varepsilon_a$ , which we choose as  $10^{-11}$  unless stated otherwise; (ii) it is no more than twice the parameter length of that of its neighbors; (iii) the length of the panel does not exceed a given fraction of the minimal radius of curvature at a point of the panel, or is less than a minimal length proportional to the target error; and (iv) any check point corresponding to a point  $\mathbf{x}$  is not closer than  $\delta - r_c$  to any point on the surface.

The second criterion ensures that the panels are the leaves of a *balanced* binary tree, which is needed for accurate evaluation of integrals at the check points. For domains with sharp corners, the forth and second conditions imply dyadic refinement of panel length bounded below by panel minimum length  $\varepsilon_l$ .

In both cases, the result is a set of  $N$  nodes  $\mathbf{x}_j = X(t_j)$ , where  $t_j$  are the parameter values of the nodes, with weights  $w_j = |X'(t_j)|w'_j$  where  $w'_j$  are the Gauss–Legendre weights scaled by the panel parametric lengths. This native quadrature approximates the boundary condition  $f$  with target accuracy  $\varepsilon_a$ . It follows from Eq. (1.6) that this also holds for the density  $\phi$ , as  $\phi$  to be no less smooth than  $f$  and  $X$ .

## 2.2 On-surface evaluation for iterative solution of the linear system

As discussed in the introduction, one context where singular quadratures are needed is for applying  $A$ , the matrix discretization of the operator  $(-\frac{1}{2}I + D)$ , to the current density vector  $\phi$  during the iterative solution of Eq. (1.8). This matrix-vector multiplication is equivalent to evaluation of the interior limit of the double-layer potential at the nodes due to the smooth interpolant of the density vector. As with QBX [34, Sec. 3.5], one may exploit this in two different ways.

- One-sided QBKIX: as stated above, we use the interior limit of the potential at the nodes for  $A\phi$ .
- Two-sided QBKIX: we average the interior and exterior limits of the potential at the nodes, which, by canceling the jump relation terms, applies a matrix approximation to the operator  $D$ . We then explicitly add  $-\frac{1}{2}\phi$  to the answer.

Although mathematically equivalent, these two variants smooth high-frequency components in the density differently: one-sided QBKIX tends to dampen these components, leading to an accumulation of eigenvalues of  $A$  around zero. This has a negative impact on convergence. In contrast, for two-sided QBKIX, since the approximation of  $D$  tends to damp high-frequency components, the explicit inclusion of  $-\frac{1}{2}I$  ensures that these components end up being multiplied by a number very close to  $-\frac{1}{2}$ , which leads to better clustering of the spectrum and improved convergence rates. We present a numerical comparison of these two alternatives in Section 4.2.



### 2.3 Efficiency considerations and computational complexity

Given a set of evaluation points  $\mathbf{x}$ , the brute-force approach is to run the algorithm described above, including construction of check and proxy points, for each sample point separately. This is highly inefficient, and the following obvious optimizations can be applied:

- The upsampled density on the fine-scale nodes need be computed only once, and each expansion center may be chosen to cover several targets; this requires increasing evaluation disk radius  $\delta$ , adjusting other parameters accordingly.
- The SVD of matrices  $Q$  may be precomputed. For translation- and scale-invariant kernels, (i.e., all kernels we consider except Yukawa and Helmholtz) these matrices do not depend on the choice of the center and circle radii, as long as the ratio  $R/r_c$  is fixed.
- One may use the kernel-independent FMM method for evaluation of the solution at the check points for all target points at once.

We consider the complexity of using QBKIX for the task of on-surface evaluation at all boundary nodes  $\mathbf{x} \in \Gamma$ . For a boundary with  $M$  panels and  $q$ -node Gauss–Legendre quadrature on each, there are  $N = Mq$  nodes in total. We use a conservative assumption that a distinct set of check and proxy points is used for each of the targets. Then, using KIFMM, the evaluation of the boundary integral from the  $\beta$ -refined boundary to the check points is  $\mathcal{O}((\beta + n_c)N)$ . We assume that the factorization of the pseudo-inverse for computing the equivalent densities  $\alpha$  is precomputed. The cost of applying the factors  $V$  and  $U^*$ , of sizes  $n_p \times k$  and  $k \times n_c$ , for targets point is  $\mathcal{O}(k(n_c + n_p)N)$ . The cost of evaluation of the approximation from proxy density values at target points is  $\mathcal{O}(Nn_p)$ .

We conclude that the overall cost is  $\mathcal{O}((\beta + n_c + kn_c + kn_p + n_p)N)$ , which for typical choices  $\beta = 4$  and  $n_c = 2n_p$  reduces to  $\mathcal{O}(kn_pN)$ . We see that the scheme is linear in  $N$ , but with a prefactor of order  $k^2$  (since, as discussed in the next section,  $n_p$  is of order  $k$ ). The two-sided variant involves another overall factor of 2.

If the same check and proxy points are used for a number of targets, an additional, potentially very large, constant-factor speedup can be obtained. The speedup factor is proportional to the average number of targets handled by each set of check and proxy points.

### 3 Error analysis and parameter choices

In this section, we present theoretical results, focusing on the cases of scalar  $u$  governed by the Laplace equation  $\Delta u = 0$  — or by the Helmholtz equation  $(\Delta + \omega^2)u = 0$  for real  $\omega$ . We expect similar results for other elliptic PDEs in Eq. (1.4).

We split QBKIX into two stages: (i) evaluation of  $u$  on the check points using a refined native quadrature, with the associated error  $e_c$ ; (ii) solution of a small linear system to determine the equivalent density values  $\alpha$  at the proxy points that best represent  $u$  at the check points. This is followed by evaluating the approximation of  $u$  at target points using these density values.

At the first stage, the error  $e_c$  is effectively the smooth quadrature error of the refined panels. The primary focus of our analysis is on the second stage. We analyze the error behavior in the idealized situation of exact arithmetic and infinitely many check points, obtaining the dependence of the second-stage error  $e$  on  $\delta$ ,  $R$ ,  $\rho$ , and  $n_p$ . We then describe a heuristic model for the effects of finite-precision computations, which adds an extra term to  $e$ , depending on  $e_c$ ,  $\delta$ ,  $r_c$ , and  $k$ .

We use the overall error model, along with experiments, to provide a choice of the various parameters in the scheme resulting in the on- and near-surface evaluation errors of the same magnitude as the far-field integration errors.

### 3.1 Error at check points

Recall that evaluation of  $u$  on the check points is done by approximating the exact integral Eq. (1.5) by Eq. (2.1) using  $q$ -node Gauss–Legendre quadrature on panels (subdivided by factor  $\beta$ ). For a flat panel, the error  $e_c$  in this evaluation is bounded by standard quadrature estimates giving a term of the form  $C_q(L/(4\beta d))^{2q}\|\phi\|_{C^{2q}}$  where  $d = \delta - r_c$  is the closest distance of check points to the panel, and  $\phi$  denotes the density for which we evaluate the integrals. Our adaptive refinement procedure ensures that the formula still holds, as the radius of curvature of the panel is larger than its length, and hence larger than  $\delta$ .

This estimate has the form of the second term in [34, Theorem 1], and for convergence as the panel length  $L$  going to zero, it requires  $L/d$  to converge to zero as well. Instead of following this route, we fix the ratio  $L/d$  to a constant, by choosing  $\delta$  and  $r_c$  as fractions of  $L$ . If  $L/(4\beta d)$  is sufficiently small, a high-order quadrature for sufficiently large  $q$  allows us to compute the integrals with any desired precision. For instance, when  $q = 16$ , it is sufficient to use  $L/(4\beta d) = 1/2$ , to obtain an error on the order of  $10^{-10}$  at distance  $d$  from the panel.

### 3.2 Error of the proxy point representation in exact arithmetic

Next, we analyze the dependence of the error (computed in exact arithmetic) of the second stage of QBKIX on the number of proxy points  $n_p$ , the proxy circle radius  $R$ , and the distance  $r$  from the center  $\mathbf{c}$  to the evaluation point. The distance  $r$  could be either smaller than  $\delta$  if targets are away from the surface, equal to  $\delta$  if  $B_\delta^c$  touches the surface at a single point, or exceed  $\delta$  if there are several on-surface targets in  $B_\delta^c$ ; we focus our attention to the case where  $r \leq \delta$ .

Let  $\hat{u}$  be given by the proxy representation, Eq. (2.4), with equivalent density values  $\alpha_j$  at proxy points  $\mathbf{y}_j$ ,  $j = 1, \dots, n_p$ . We consider evaluation of the approximation  $\hat{u}$  in  $B_r^c$ , the disc of radius  $r$  centered at  $\mathbf{c}$ , given correct values for  $u$  at a very large number of check points  $n_c$ , so that we can replace the discrete least-squares problem we solve with a continuous one.

Let the equivalent densities  $\alpha_j$  be chosen to minimize the  $L^2$  error on the check circle, i.e.,

$$\boldsymbol{\alpha} = \arg \min_{\boldsymbol{\alpha} \in \mathbb{C}^{n_p}} \|\hat{u} - u\|_{L_2(\partial B_r^c)} . \quad (3.1)$$

By convergence of the periodic trapezoidal quadrature on the check points, this corresponds to the  $n_c \rightarrow \infty$  limit of the QBKIX scheme. Let

$$e(r) := \sup_{\mathbf{x} \in \partial \Omega \cap B_r^c} |\hat{u}(\mathbf{x}) - u(\mathbf{x})| , \quad (3.2)$$

be the upper bound on the pointwise error in the part of the disc lying inside the closure of the domain. We have the following bounds on  $e$  when  $u$  is sufficiently regular, meaning that any singularities in the continuation of  $u$  is further than some distance  $\rho > \delta$  from the center of the expansion  $\mathbf{c}$ .

**Theorem 3.1** *Let  $u$  be continuable as a regular solution to the Laplace or Helmholtz equation in the closed disc of radius  $\rho$  centered at  $\mathbf{c}$ . Let  $R > \delta$  in the Laplace case. Let the QBKIX equivalent density values at proxy points be solved in exact arithmetic in the least-squares sense on the check circle as in Eq. (3.1), and let  $e$  be defined by Eq. (3.2) where  $\hat{u}$  is the expansion in Eq. (2.4). Then, in a disc of radius  $r$*

$$e(r) \leq \begin{cases} C \left(\frac{r}{\rho}\right)^{n_p/2}, & \rho r < R^2, \\ C \sqrt{n_p} \left(\frac{r}{R}\right)^{n_p}, & \rho r = R^2, \\ C \left(\frac{r}{R}\right)^{n_p}, & \rho r > R^2, \end{cases} \quad (3.3)$$

where in each case,  $C$  indicates a constant that may depend on  $u$  (and  $\omega$  in the Helmholtz case),  $\mathbf{c}$ ,  $r$ , and  $R$  but not on  $n_p$ .

*Proof* Following the technique of Barnett and Betcke [4, Theorem 3], we only need to show that there exists some choice of density values  $\alpha$  for which the estimate holds; the least-squares solution cannot be worse than this. We choose density values  $\alpha$  to cancel the Fourier coefficients with frequency  $|n| < n_p/2$  of the pointwise error  $\hat{u} - u$  on the check circle.

By uniqueness of the local expansion for the regular PDE solution (in polar coordinates,  $\sum_{n \geq 0} a_n r^n e^{in\theta}$  for Laplace or  $\sum_{n \in \mathbb{Z}} a_n J_n(\omega r) e^{in\theta}$  for Helmholtz) this choice of density values also cancels the same Fourier coefficients on any circle centered at  $\mathbf{c}$  with radius less than  $R$ . Applying [4, Theorem 3] for the Helmholtz case, the  $L^2$ -norm of the error on the circle of radius  $r$  obeys a bound of the form Eq. (3.3). Barnett and Betcke [4, Section 2.1] produce the Laplace case as a limit of the Helmholtz case; however, one also needs the result that the constant single-layer density generates the constant potential  $\log R/r_c$ , which excludes  $R = r_c$  because it can only produce zero-mean data on the circle.

Finally, we need to show that the sup norm of the error on the circle of radius  $r$  is bounded by the  $L^2$ -norm; this holds since the error  $\hat{u} - u$  is a regular PDE solution in a disc with radius strictly larger than  $r$ , namely  $B_{\min(R, \rho)}^c$ . Thus, its Fourier coefficients on the  $r$ -circle decay exponentially in  $|n|$ , and are thus summable with a bound controlled by the  $L^2$  norm. In the case where  $B_r^c$  lies partially outside  $\Omega$ , one may continue  $u$  as a regular PDE solution in the disc and apply the above.  $\square$

*Remark 3.1* The above derivation relies on analysis from the literature on the method of fundamental solutions (MFS). The original result for the Laplace equation is due to Katsurada [32, Theorem 2.2], which considers the case  $n_c = n_p$  and restricted to  $r = r_c$ . We extend this result to include *extrapolation* from the check radius  $r_c$  out to larger radii  $r$ .

Remarkably,  $r_c$  does not appear in Eq. (3.3), because in exact arithmetic it does not matter at what radius the Fourier coefficients are matched. In the next section we will see that in practice rounding error strongly affects the choice of  $r_c$  since the extrapolation is ill-conditioned.

A surprising aspect of Theorem 3.1 is that  $u$  may have singularities *closer* to the center than the proxy radius  $R$  and yet exponential convergence still holds; this is closely related to the Runge approximation theorem.

*Remark 3.2* The two regimes in Eq. (3.3) may be interpreted as follows:

- $r < \frac{R^2}{\rho}$ : the solution  $u$  is relatively rough (has a nearby singularity), and error is controlled by the decay of the local expansion coefficients  $a_n$  of  $u$  for orders beyond  $n_p/2$ .
- $r > \frac{R^2}{\rho}$ : the solution  $u$  is smooth, and error is controlled instead by aliasing (in Fourier coefficient space) due to the discreteness of the proxy point representation on the proxy circle.

We observe in numerical experiments that when the boundary is adaptively refined based on the boundary data as in Section 2,  $L \approx \rho$  and the expansion centers that dominate the error in a domain are typically those that are near to a singularity of the solution. Such centers are typically in the rough regime.

Note that the boundary  $\Gamma$  may intersect the closed disc, and still  $u$  may be continued as a PDE solution into the closed disc. This requires the boundary data  $f$  or density to be analytic — see [3] for related analysis of QBX in this case.

*Remark 3.3 (Extension of analysis to other kernels)* It is clearly of interest to have a kernel-independent extension of Theorem 3.1 that would apply also to vector PDEs such as Stokes. Initial attempts suggest this requires significantly more complicated analysis, since to use the method of the above proof one needs to be able to write down a proxy coefficient vector  $\alpha$  that produces a single Fourier mode on the check circle plus exponentially decaying amounts of aliased modes, which is challenging even in the Stokes case. We leave this for future work.

### 3.3 Modeling the effect of finite-precision arithmetic

Independence from  $r_c$  in Theorem 3.1 relies on exact arithmetic; since the extrapolation from  $r_c$  to a larger  $r$  is ill-conditioned. Moreover, due to finite precision, there are possibly fewer than  $n_p$  functions available to cancel the Fourier coefficients. As a result, we need to study the effect of rounding error on  $\hat{u} - u$ . Rather than attempting a rigorous analysis, we present a heuristic model and demonstrate that it agrees well with numerical observations.

We first show that the  $n^{\text{th}}$  singular value of the matrix  $Q$  in Eq. (2.2) decays as  $\frac{1}{n}(r_c/R)^{n/2}$ , i.e., marginally faster than exponentially. In the continuous limit ( $n_p, n_c \rightarrow \infty$ ), this corresponds to the decay of the eigenvalues of the single-layer operator with kernel  $\Phi$ , whose eigenfunctions are the Fourier modes, since the operator is convolutional. For the Laplace equation, the potential defined in polar coordinates centered at  $c$  as

$$v(r, \theta) = \begin{cases} (R/2n)(r/R)^n e^{in\theta}, & r \leq R, \\ (R/2n)(r/R)^{-n} e^{in\theta}, & \text{otherwise}, \end{cases}$$

solves the PDE everywhere except at  $r = R$ , where the jump in radial derivative is  $e^{in\theta}$ . We conclude that  $v$  is the single-layer potential due to the  $n^{\text{th}}$  Fourier mode density. Substituting  $r = r_c$ , and recalling that the  $n^{\text{th}}$  singular value is eigenvalue for the frequency  $n/2$ , as the frequencies are in the range  $-n/2$  to  $n/2$ , we conclude that  $\sigma_n = \frac{1}{n}(r_c/R)^{n/2}$ .

The above argument also applies for the Stokes case except due to having two vector components,  $n^{\text{th}}$  singular value of matrix  $Q$  corresponds to the eigenvalue for frequency  $n/4$ . The Helmholtz case — although there are  $\mathcal{O}(\omega)$  eigenvalues that do not decay — is asymptotically identical to Laplace [4, Equation (14)]. To verify this asymptotic behavior, in Fig. 3.1 we show the decay of singular values for several kernels.

When the pseudoinverse of  $Q$  is computed based on Eq. (2.5), only  $k$  singular values lying above  $\varepsilon_{\text{pinv}}\sigma_1$  are retained. The corresponding singular vectors approximate the lowest Fourier modes up to frequency  $|n| < k/2$  (in the scalar PDE cases). Thus, equating up to constants the  $k^{\text{th}}$  singular value above to  $\varepsilon_{\text{pinv}}$ , the ranks of the matrices in the pseudoinverse are

$$k \approx \min(k_m, n_p), \quad k_m = 2 \frac{\log(1/\varepsilon_{\text{pinv}})}{\log(R/r_c)}, \quad (3.4)$$

and the highest (Nyquist) frequency they can represent is  $k/2$ .

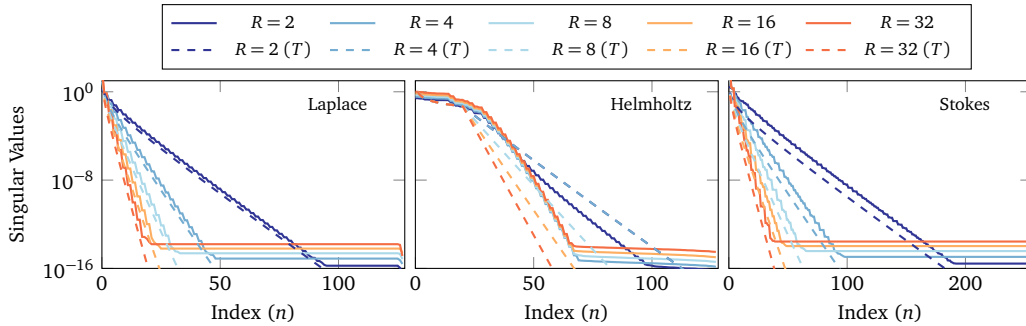


**Fig. 3.1:** SINGULAR VALUES OF PROXY TO CHECK MATRIX. The solid lines are the singular values of  $Q$  for different  $R$  and different single-layer kernels, and the dashed lines labeled (T) are the theoretical decay:  $\frac{1}{n}(r_c/R)^{n/2}$  for Laplace or Helmholtz, and  $\frac{1}{n}(r_c/R)^{n/4}$  for Stokes, where  $n$  denotes the index of the singular value. Other parameters are  $r_c = 1$ ,  $n_p = 128$ ,  $n_c = 256$ . For the Helmholtz problem, the dashed lines show the asymptotic bound for the singular values and are not accurate for small indices; the interested reader is referred to [4, Eq. (14)].

The values of  $\tilde{u}$  at the check points have error bounded by  $e_c$ , so in this model we expect the errors to be amplified (by considering the local expansion as above) to become  $e_c(r/r_c)^{k/2}$  at the evaluation radius  $r$ .

### 3.4 Error bounds and optimal parameter choices

Combining the results from Sections 3.2 and 3.3 for a kernel-independent expansion, using  $n_p$  proxy points, the error is bounded by

$$e(r) \leq \begin{cases} C \left(\frac{r}{\rho}\right)^{k/2} + Ce_c \left(\frac{r}{r_c}\right)^{k/2}, & \rho r < R^2, \\ C \left(\frac{r}{R}\right)^{n_p} + Ce_c \left(\frac{r}{r_c}\right)^{k/2}, & \rho r > R^2, \end{cases} \quad (3.5)$$

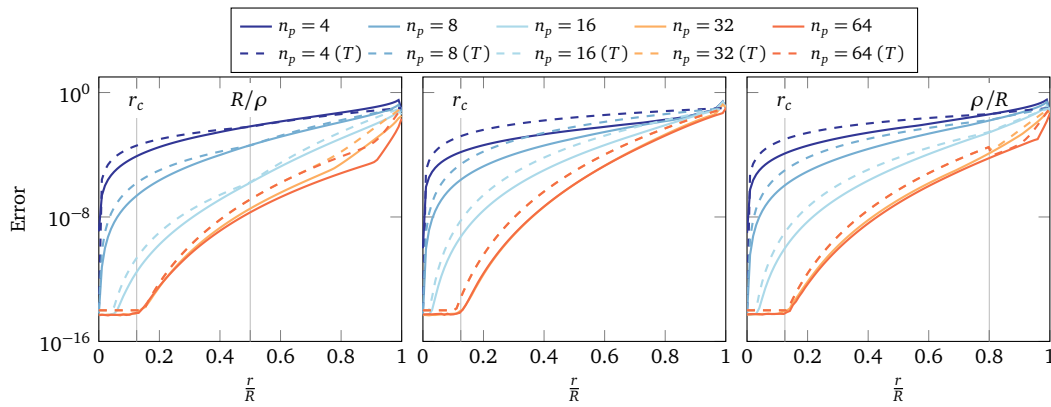
where  $C$  represents possibly different constants in each case (omitting the case  $\rho r = R^2$ ).

In Fig. 3.2, we show how this formula models the error growth for a single kernel-independent expansion interpolating a Laplace solution in free space with a known nearest singularity at various distances  $\rho$ , for a typical choice of ratio  $R/r_c = 8$ . The key observation is that, despite its simplicity, our model Eq. (3.5) explains well the observed error behavior. Other salient features of the plots include:

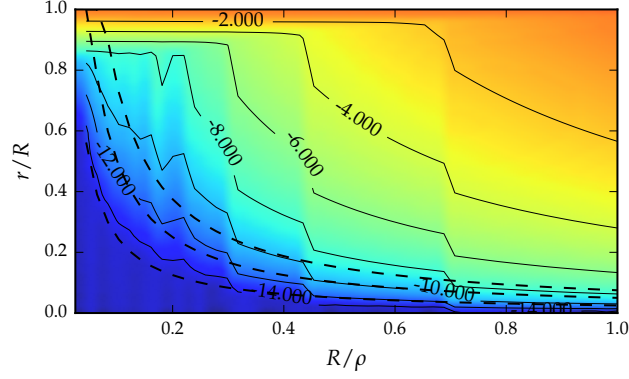
- As  $r$  increases beyond  $r_c$ , errors grow rapidly dominated by the second term in the error estimate.
- The error is mostly controlled by  $k$  and increasing  $n_p$  beyond  $k_m \approx 27$  (defined in Eq. (3.4)) has no tangible effect unless  $\rho r > R^2$  (i.e., right half of left plot).

Figure 3.3 instead continuously varies  $R/\rho$  (the inverse scaled singularity distance), showing the same effect: a relatively distant singularity allows high accuracy expansion out to larger  $r/R$ .

**Choice of parameters.** Using the model Eq. (3.5), one can make choices for  $R$ ,  $r_c$ ,  $\delta$ , and  $n_p$  to achieve a desired accuracy  $\varepsilon$ . An unknown in applying this in a practical setting is the singularity distance  $\rho$ . However, in any high-accuracy choice of boundary quadrature, such as the adaptive panel quadrature of Section 2, panels are refined such that the data  $f$  and hence the density  $\phi$  and the solution  $u$  are smooth



**Fig. 3.2:** ERROR BOUNDS FOR LAPLACE QBKIX WITH KNOWN SINGULARITY. Errors  $e$  observed (solid lines) and predicted by Eq. (3.5) (dashed lines) for a single expansion with different singularity distances  $\rho = 2R, R$ , and  $0.8R$ , and different numbers of proxy points  $n_p$ . The expansion is centered at  $\mathbf{c} = [0, 0]$  and the solution  $u(\mathbf{x}) = -\log|\mathbf{x} - \mathbf{x}_0|$ ,  $\mathbf{x}_0 = \rho e^{1i/19}$  is a harmonic function with a singularity at distance  $\rho$ . Laplace single-layer kernel is used for the expansion. The error is the maximum error over the  $B_r^c$  as defined in Eq. (3.2). The proxy to check radius ratio is  $R/r_c = 8$ , the number of checks is set to  $n_c = 2n_p$ ,  $e_c = 10^{-14}$ , and  $k_m \approx 27$  (given by Eq. (3.4) with  $\varepsilon_{\text{pinv}} = 10^{-14}$ ). The constants  $C$  in Eq. (3.5) were chosen to qualitatively match the trend lines (all set to 0.1).



**Fig. 3.3:** ERROR AT DIFFERENT EVALUATION RADII. The error for evaluation of a single expansion with various  $R$  and  $r$ , but fixed  $r_c = \rho/40$  and  $\rho$ . The expansion is interpolating a harmonic function (similar to the one used in Fig. 3.2) with singularity at distance  $\rho = 4$ , using the Laplace double-layer kernel. The dotted lines are  $r = mr_c$  for  $m = 1, 2$ , and  $3$ . In practice, we have no direct control on  $\frac{R}{\rho}$ , and it is implied by the panel size. Here we chose  $n_p = 64$ , and  $n_c = 2n_p$ ; the trends are the same for lower  $n_p$  and  $n_c$ .

on the local panel scale  $L$ , thus we expect singularities to be at least of order  $L$  distant from the center. Indeed, we experimentally observe (in tests where we know the location of singularity, e.g., Fig. 3.4 or Section 4.3) that when the panels are adaptively refined,  $L < \rho$ , and consequently the convergence behavior is most like the left-hand plot of Fig. 3.2.

Given the target accuracy of  $\varepsilon$  for the solution and the selected native quadrature order  $q$ , the adaptive refinement of boundary sets the panel length  $L$ . We use the following steps to glean the value of other parameters. Since the constants in the error estimates are problem dependent and unknown, we set them to unity. To have a concrete example, we pick  $\varepsilon = 10^{-10}$  and  $q = 16$ .

- (1) **Setting  $\delta$ :** By construction, points farther than  $2\delta$  from the boundary are evaluated using the native quadrature. To meet the desired error  $\varepsilon$  at these points,  $\frac{L}{\delta} \approx 8\varepsilon^{1/2q}$ , which implies  $\delta \approx L/4$  for  $\varepsilon = 10^{-10}$ ,  $q = 16$ .
- (2) **Setting  $k_m$ ,  $R/r_c$ , and  $n_p$ :** Requiring that the two terms in the error estimate (i.e., proxy point representation and extrapolation errors) have similar contribution at the on surface point ( $r = \delta$ ) and assuming that  $L \approx \rho$  we can estimate the minimum required  $k$  based on the proxy representation error in the rough regime:

$$\left(\frac{\delta}{\rho}\right)^{k/2} \approx \varepsilon \quad \text{or} \quad k \approx \frac{2 \log \varepsilon}{\log(\delta/L)}, \quad (3.6)$$

implying  $k \approx 32$  for  $L/\delta = 4$ ,  $\varepsilon = 10^{-10}$ . Since  $k$  is bounded by  $\min(k_m, n_p)$ , knowing minimum  $k$  implies a lower bound for  $k_m$  and  $n_p$ . Therefore, reorganizing Eq. (3.4), we have  $R/r_c = \varepsilon_{\text{pinv}}^{2/k} \approx 7$ , for  $\varepsilon_{\text{pinv}} = 10^{-14}$ .

- (3) **Setting  $r_c/\delta$  and  $\beta$ :** Inspecting the extrapolation error at an on surface point, we have

$$e_e(\delta) \approx e_c \left(\frac{\delta}{r_c}\right)^{k/2} \approx \left(\frac{L}{4\beta(\delta - r_c)}\right)^{2q} \left(\frac{\delta}{r_c}\right)^{k/2} \approx \left(\frac{L}{4\beta\delta}\right)^{2q} \frac{1}{(1 - \theta)^{2q} \theta^{k/2}}, \quad (3.7)$$

where  $\theta = r_c/\delta$ . This expression attains its minimum at  $\theta = \frac{k}{4q+k}$ . For  $q = 16$  and  $k = 32$ , we have  $\theta = 1/3$ . As we require that two terms in the error estimate have similar contribution, we use  $e_e(\delta)$  and estimate  $\beta$ :

$$\beta \approx \frac{L/4\delta}{(1 - \theta)\theta^{k/4q}\varepsilon^{1/2q}}, \quad (3.8)$$

implying  $\beta = 5$ , for the choices of parameter listed above.

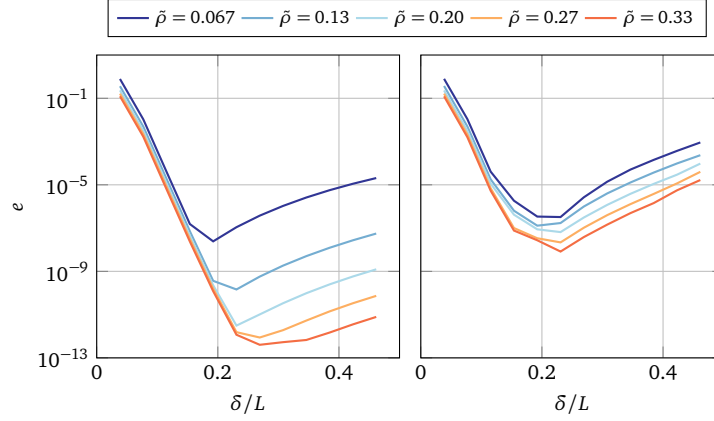


**Fig. 3.4:** ERROR VS. CENTER AND SINGULARITY DISTANCES. The induced error for singularities and centers at various distances from the boundary for the Laplace Dirichlet interior BVP, in the domain shown in Fig. 4.2. The boundary data is generated by putting a Laplace singularity at distance  $\tilde{\rho}$  from the boundary—the singularity distance to the center of expansion is  $\rho \geq \tilde{\rho} + \delta$ . The density is solved directly and QBKIX is used only for evaluation. The error is computed using the known solution corresponding to the boundary data. The left plot shows the errors for the case with fixed number of panels on the boundary ( $M = 40$  panels). In this plot, because  $L$  is fixed,  $L/\tilde{\rho}$  is decreasing by increasing  $\tilde{\rho}$ . The right plot shows the errors for adaptive refinement of the boundary with  $\epsilon_a = 10^{-11}$ . Here, since  $L$  is chosen adaptively due to the boundary data, it increases as the solution becomes smoother. Because,  $L$  is chosen proportional to  $\tilde{\rho}$ , the error curves almost collapse to one. We use  $n_p = 64$ ,  $n_c = 2n_p$ ,  $r_c = \delta/3$  and  $R = 8r_c$ . In both cases, the center of expansion is located based on the panel size at distance  $\delta$ .

Note that we have not analyzed the effect of finite  $n_c$ , but find that the choice  $n_c = 2n_p$  behaves indistinguishably from the limit  $n_c \rightarrow \infty$ ; we attribute this to the rapid convergence of the periodic trapezoid rule on the check points.

## 4 Numerical experiments

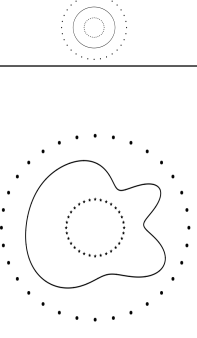
In this section, we present the results of numerical tests demonstrating the accuracy and versatility of the QBKIX algorithm for on-surface evaluation needed for the boundary integral equation solver and solution evaluation close to the surface. In the following experiments, unless noted otherwise, we use QBKIX for both tasks.

### 4.1 Convergence with respect to the number of panels

In Table 4.1, we report the convergence of the solution evaluated at the interior points using non-adaptive boundary quadrature with increasing number of panels. The test solution is the potential due to a set of singularities at the source points shown outside the domain. These source points are used to generate the boundary data  $f$  and the reference solution to check the error. For all problems, the double-layer formulation is used, except for the Helmholtz for which a combined-field formulation  $u = \mathcal{D}[\phi] + i\omega\mathcal{S}[\phi]$ , where  $\mathcal{S}$  is the single-layer potential [14, Section 3.2], is used. This representation addresses problems associated with resonance of the complementary domain. The double-layer (or combined-field) density  $\phi$  is solved using QBKIX to evaluate the matrix-vector product in each iteration of GMRES. The error in the density is quantified by computing the solution from  $\phi$ , Eq. (1.5), at a set of target points in the interior of the domain. For the first three kernels, which are smooth, we also report the convergence using the Nyström (*direct*) evaluation, Eq. (1.9), which by comparison against one- or two-sided QBKIX shows how much of the error is due to QBKIX.

In all cases, it can be seen that QBKIX gives high-order convergence rate that is independent of the type of the kernel. We notice that the error performance of the two-sided variant is worse than one-



Geometry	Kernel	Quadrature	Absolute error (Number of panels)			
	Laplace	Direct	2.90e−06 (2)	9.46e−10 (4)	6.42e−14 (6)	1.98e−14 (8)
		QBKIX (one)	3.39e−06 (2)	9.69e−10 (4)	4.46e−12 (6)	3.54e−12 (8)
		QBKIX (two)	2.25e−05 (2)	4.07e−07 (4)	2.24e−08 (6)	2.37e−09 (8)
	Laplace	Direct	5.80e−07 (6)	8.52e−07 (8)	1.67e−09 (10)	5.65e−12 (12)
		QBKIX (one)	2.49e+00 (6) <sup>1</sup>	1.32e−04 (8)	4.62e−09 (10)	3.09e−09 (12)
		QBKIX (two)	4.29e−01 (6)	3.06e−04 (8)	4.25e−07 (10)	1.50e−07 (12)
	Stokes	Direct	1.48e−04 (6)	6.67e−05 (8)	6.51e−08 (10)	6.06e−10 (12)
		QBKIX (one)	2.89e−08 (20)	4.78e−09 (24)	1.73e−09 (28)	6.38e−10 (32)
		QBKIX (two)	6.95e−06 (16)	4.87e−08 (32)	3.31e−09 (48)	9.45e−10 (64)
	Helmholtz <sup>2</sup> ( $\omega = 2$ )	QBKIX (one)	2.12e−04 (8)	1.20e−09 (12)	4.22e−10 (16)	2.09e−11 (20)
		QBKIX (two)	3.97e−04 (8)	1.91e−07 (12)	3.42e−08 (16)	7.92e−09 (20)
	Yukawa ( $\lambda = 2$ )	QBKIX (one)	1.60e−04 (8)	6.42e−07 (12)	3.84e−09 (16)	1.48e−09 (20)
		QBKIX (two)	5.44e−04 (8)	1.27e−07 (12)	2.19e−08 (16)	4.79e−09 (20)
	Elastostatic ( $\nu = 0.1$ )	QBKIX (one)	2.07e−03 (8)	7.16e−06 (12)	4.35e−07 (16)	7.19e−07 (20)
		QBKIX (two)	3.17e−02 (8)	1.27e−05 (12)	2.26e−06 (16)	6.77e−07 (20)

1 When there are a few panels on the boundary, a check circle may be placed near other panels which adversely affects the error.

2 For Helmholtz equation, we use a combined field formulation.

**Table 4.1:** SOLUTION CONVERGENCE VS. NUMBER OF PANELS. *Error in the solution to interior Dirichlet boundary value problems using non-adaptive  $M$ -panel quadrature and QBKIX for solution. The subplots show  $\Gamma$  (solid) and the exterior sources used to generate the solution, and interior test points. There are 40 source points outside the domain and error is measured on 40 points inside. The error is the maximum of absolute error over these interior points. The numerical parameters are  $n_p = 32$ ,  $n_c = 2n_p$ ,  $R = 8r_c$ , and  $\delta = 3r_c$ . “Direct” indicates usage of the quadrature of Eq. (1.9) instead of QBKIX for the linear solve. “One” and “two” indicate one- or two-sided versions of on-surface QBKIX discussed in Section 2.2.*

sided at the same number of panels (however, as we discuss below, it is valuable since it improves the convergence rate of GMRES).

## 4.2 Operator spectrum and GMRES convergence rate

We now perform numerical tests of the one-sided and two-sided variants of on-surface evaluation of QBKIX discussed in Section 2.2 and compare it to direct use of an accurate quadrature. To simplify comparisons, we use an operator with a smooth kernel (Laplace). The spectra and convergence behavior for singular kernels is similar. In Fig. 4.1 we plot — for the domain shown in Fig. 4.2 and the Laplace equation — the eigenvalues for four different approximations to the operator  $-\frac{1}{2} + D$ : one-sided (interior) QBKIX, the one-sided (exterior) QBKIX, two-sided QBKIX, and the quadrature given by Eq. (1.9), to which we refer as *direct*. The exterior version of QBKIX is constructed similarly to the interior variant discussed in Section 2. The only modification is that for each collocation point  $\mathbf{x}_0$  on  $\Gamma$ , we place an expansion center at  $\mathbf{c} = \mathbf{x}_0 + \delta \mathbf{n}$ . We see that the one-sided variants have clusters of eigenvalues near zero, whereas the two-sided variant and the Nyström matrix have a cleaner spectrum with eigenvalue clustering only around  $\frac{1}{2}$ .

A broader spread of the eigenvalues has a negative impact on GMRES convergence [40]. Fig. 4.1, right, shows GMRES residual versus the iteration number for the interior, two-sided, and direct operators with two different right-hand sides (boundary data corresponding to a harmonic function and a random right-hand side).

The convergence of one-sided interior QBKIX is identical to the Nyström method convergence up to the residual magnitude on the order of numerical accuracy of QBKIX, but it slows down once the residual decreases below this value (near  $10^{-9}$ ). The two-sided variant has identical convergence behavior to the direct method, and converges in a few iterations. We also show the residual for a random-right hand side to expose the effect of near-zero eigenvalues: we see that convergence is very slow for the one-sided scheme in this case, but for the two-sided scheme it is the same as for the true smooth data  $f$ .

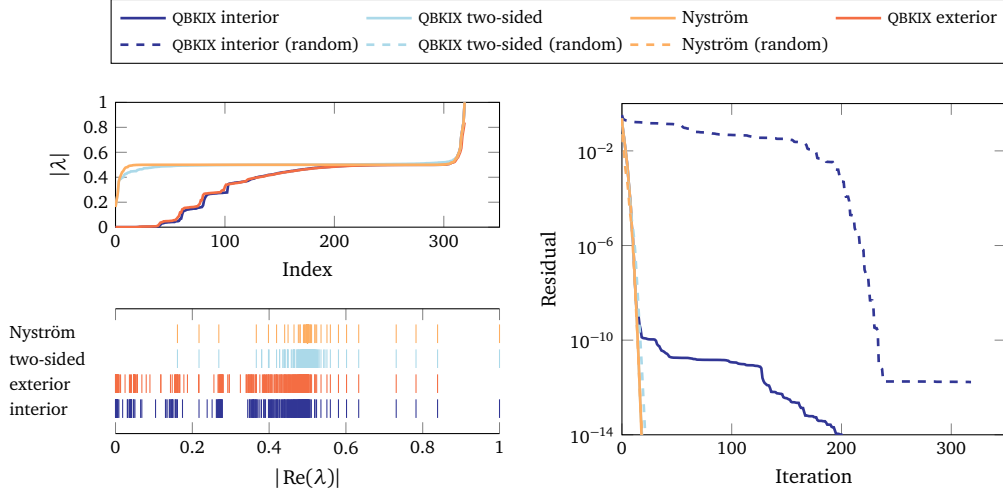


**Fig. 4.1:** THE SPECTRA OF DISCRETIZATIONS OF THE LAPLACE DOUBLE-LAYER OPERATOR. This figure shows eigenvalues, and the GMRES convergence rate, for different discretizations of the Laplace double-layer operator in the domain shown in Fig. 4.2. The left plots show the real part and the magnitude of the eigenvalues corresponding the one-sided interior QBKIX, one-sided exterior QBKIX, two-sided QBKIX, and the plain Nyström matrix. See Sections 2.2 and 4.2. The right plot shows the residual versus the iteration number for the three interior variants with two different right hand sides (boundary data corresponding to a harmonic function or random data). The residual of the two-sided and Nyström schemes are indistinguishable.

#### 4.3 Error for Dirichlet problems for five PDEs

For this set of tests, we use adaptive refinement as described in Section 2. We use QBKIX both as the on-surface quadrature scheme when solving for the desired density as well as the evaluator for the near-singular integrals. As before, we use boundary data sampled from a sum of fundamental solutions centered at a set of points close to the boundary. Fig. 4.2 plots the error across the domain for all of the PDEs listed in Eq. (1.4), on the points lying on a  $600 \times 600$  grid and interior to the domain. When an evaluation point is within  $2\delta$  distance from the boundary, it is evaluated using the nearest QBKIX expansion. The remaining points are evaluated using Eq. (1.7) applied to Eq. (1.5).

We observe that parameter choices which were selected for the Laplace equation perform well for the other PDEs. As expected, the highest error is due to expansions for panels adjacent to larger ones (e.g. Fig. 4.2(a)).

#### 4.4 Domain with a large number of corners

As a final example, we use QBKIX in a domain with 256 corners as shown in Fig. 4.3. A Laplace boundary value problem is solved using GMRES with tolerance for relative residual set to  $\varepsilon_r = 10^{-6}$ . The boundary condition is generated similar to the examples in Section 4.3 by placing 32 source points on a circle with radius 0.75 centered at  $[0.5, 0.5]$  (the domain's bounding box is  $[0, 1] \times [0, 1]$ ).

The boundary of the domain is adaptively refined, with minimum panel length set to  $\varepsilon_l = \varepsilon_r/10$ . Large panels are also refined based on the adaptive criterion we outlined in Section 2. The dyadic and adaptive refinements result in a total of 9560 panels.

Due to the singularities on the boundary, the system matrix is ill-conditioned. The ill-conditioning is greatly reduced using left and right preconditioners with square root of smooth quadrature weights on its diagonal [9], solving for density in  $L^2$  sense. Considering this preconditioning and since the last panel in each side of the corner is of length smaller than  $\varepsilon_r/10$ , we set the density on those panels to zero (effectively deleting the last two panels). The GMRES converges after 33 iterations; we use KIFMM (with accuracy set to  $\varepsilon_r/10$ ) for fast evaluation.

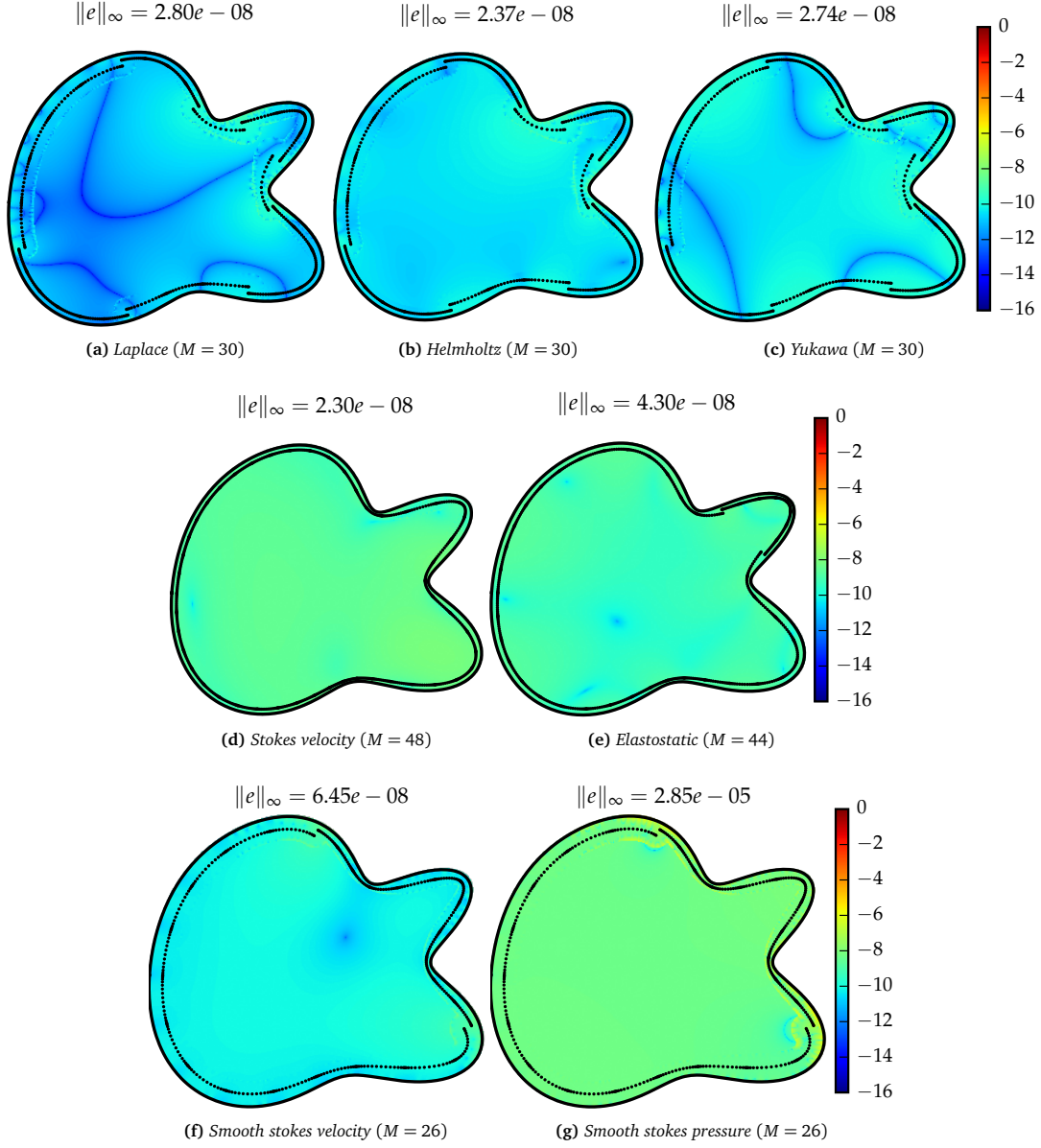


**Fig. 4.2:** THE  $\log_{10}$  OF POINTWISE ERROR. The interior Dirichlet boundary value problem is solved with known solution generated by source points distributed over an exterior circle as shown in the lower figure in Table 4.1, apart from in (f) and (g) where we use the cubic flow with velocity  $\mathbf{u} = [y^3, x^3]$  and pressure  $p = 6xy$ . Error is evaluated on the same fine grid used for visualization ( $600 \times 600$ ). We use  $q = 16$  node Gauss–Legendre panels and set  $\varepsilon_a = 10^{-13}$  in the adaptive panel quadrature set-up.  $M$  denotes the number of boundary panels. The expansion centers  $\mathbf{c}$  are shown by black dots close to the boundary.

## 5 Conclusions

In this paper we introduced a new quadrature scheme for the high-order accurate evaluation of layer potentials associated with general elliptic PDE on the domain boundary and close to it. The scheme—which builds local solution approximations using a refined evaluation and the solution of small linear systems—relies solely on the evaluation of the underlying kernel, so is essentially PDE-independent. It is highly flexible, being agnostic as to the boundary condition type, the layer representation, and crucially, the dimension of the problem. We have analyzed the error behavior of the scheme for Laplace and

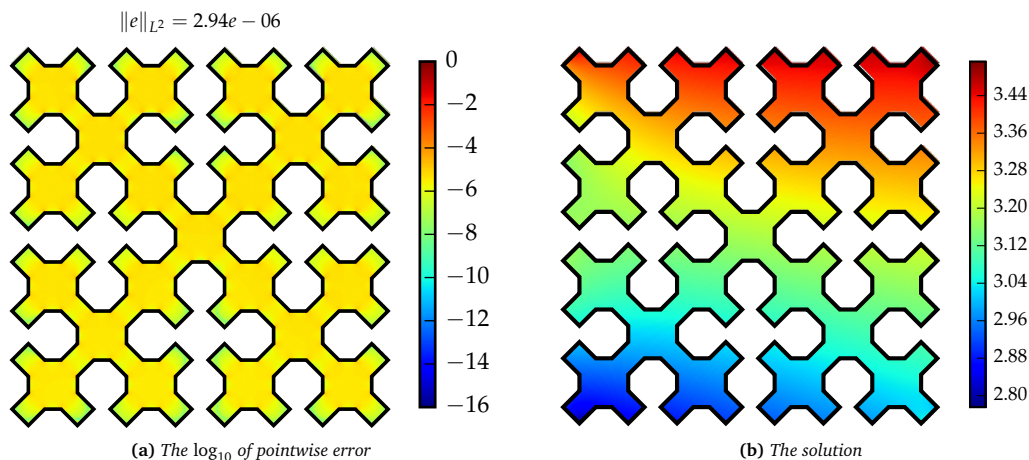


Fig. 4.3: QBKIX IN A DOMAIN WITH 256 CORNERS.

Helmholtz cases. It also fits naturally in the framework of existing fast kernel-independent algorithms for potential evaluation such as the KIFMM, as it uses similar local approximations.

We have tested its accuracy for three scalar- and two vector-valued 2D Dirichlet boundary-value problems that are common in engineering problems. We have not attempted to optimize performance, and leave that for future work.

There are several obvious extensions that have motivated this initial study that we plan to pursue:

- (1) Generalization to 3D. High-order singular quadratures for surfaces are complicated, application dependent, and scarce. Since it requires only pointwise kernel evaluations, QBKIX is by design very easy to implement in 3D using proxy and check surfaces, and would handle a wide class of PDEs. The constants will be larger, but the linear systems (anticipated to be of size around  $10^3$ ) would still be very practical.
- (2) Generalization to other boundary conditions. QBX, and thus also QBKIX, can apply without modification, for instance, the normal derivative of the double-layer operator, which is hypersingular.
- (3) Integration with KIFMM. In this work, we only used kernel-independent FMM for fast evaluation of potential on the check points. However, we expect performance gains by reusing the local expansion of KIFMM as a QBKIX expansion.
- (4) Local QBKIX. The construction of local schemes which automatically handle general domains with thin features (i.e., with geodesically distant parts of the boundary in close proximity in space) without excessive refinement needed for the panel size to be on the order of feature size, is important for making the method practical. [3] proposed the *local* version of QBX, in which only the contribution of the nearby panels to a target is evaluated using expansions, while contributions of more distant panels is evaluated using standard quadrature. Implementing this idea is nontrivial however, as the end-points of the group of neighboring panels produce new singularities that can affect the convergence rate.
- (5) Generalization of analysis to all kernels. As Remark 3.3 discusses, this is a nontrivial missing piece in the theoretical foundations.

**Acknowledgements** We extend our thanks to Manas Rachh, Andreas Klöckner, Michael O’Neil, and Leslie Greengard for stimulating conversations about various aspects of this work. A.R. and D.Z. acknowledge the support of the US National Science Foundation (NSF) through grant DMS-1320621; A.B. acknowledges the support of the NSF through grant DMS-1216656.

## Appendix A List of kernels

Here we list the kernels for the single- and double-layer potentials for the PDEs considered text. In each case  $\mathbf{x}$  and  $\mathbf{y}$  are points in  $\mathbb{R}^2$  and  $\mathbf{r} := \mathbf{x} - \mathbf{y}$ . The single-layer kernel is the fundamental solution. In double-layer kernels,  $\mathbf{n}$  is the unit vector denoting the dipole direction, which in the context of boundary integral formulation is the outward pointing normal to the surface.

- Laplace:

$$\Delta u = 0, \quad (\text{A.1})$$

$$S(\mathbf{x}, \mathbf{y}) = -\frac{1}{2\pi} \log |\mathbf{r}|, \quad (\text{A.2})$$

$$D(\mathbf{x}, \mathbf{y}) = \frac{1}{2\pi} \frac{\mathbf{r} \cdot \mathbf{n}}{|\mathbf{r}|^2}, \quad (\text{A.3})$$

$$\lim_{\mathbf{y} \rightarrow \mathbf{x}} D(\mathbf{x}, \mathbf{y}) = -\frac{\kappa}{4\pi}, \quad \mathbf{x}, \mathbf{y} \in \Gamma, \quad (\text{where } \kappa \text{ is the signed curvature}). \quad (\text{A.4})$$

- Yukawa:

$$\Delta u - \lambda^2 u = 0, \quad (\text{A.5})$$

$$S(\mathbf{x}, \mathbf{y}) = \frac{1}{2\pi} K_0(\lambda |\mathbf{r}|), \quad (\text{A.6})$$

$$D(\mathbf{x}, \mathbf{y}) = \frac{\lambda}{2\pi} \frac{\mathbf{r} \cdot \mathbf{n}}{|\mathbf{r}|} K_1(\lambda |\mathbf{r}|), \quad (\text{A.7})$$

where  $K_0, K_1$  are modified Bessel functions of the second kind of order zero and one, respectively.

- Helmholtz:

$$\Delta u + \omega^2 u = 0, \quad (\text{A.8})$$

$$S(\mathbf{x}, \mathbf{y}) = \frac{i}{4} H_0^1(\omega |\mathbf{r}|), \quad (\text{A.9})$$

$$D(\mathbf{x}, \mathbf{y}) = \frac{i\omega}{4} \frac{\mathbf{r} \cdot \mathbf{n}}{|\mathbf{r}|} H_1^1(\omega |\mathbf{r}|), \quad (\text{A.10})$$

where  $H_0^1, H_1^1$  are respectively modified Hankel functions of the first kind of order zero and one.

- Stokes:

$$-\Delta \mathbf{u} + \nabla p = 0, \quad \nabla \cdot \mathbf{u} = 0, \quad (\text{A.11})$$

$$S(\mathbf{x}, \mathbf{y}) = \frac{1}{4\pi} \left( -\log |\mathbf{r}| + \frac{\mathbf{r} \otimes \mathbf{r}}{|\mathbf{r}|^2} \right), \quad (\text{A.12})$$

$$D(\mathbf{x}, \mathbf{y}) = \frac{\mathbf{r} \cdot \mathbf{n}}{\pi} \frac{\mathbf{r} \otimes \mathbf{r}}{|\mathbf{r}|^4}, \quad (\text{A.13})$$

$$\lim_{\mathbf{y} \rightarrow \mathbf{x}} D(\mathbf{x}, \mathbf{y}) = -\frac{\kappa}{2\pi} \mathbf{t} \otimes \mathbf{t}, \quad (\text{A.14})$$

$$P(\mathbf{x}, \mathbf{y}) = -\frac{1}{\pi |\mathbf{r}|^2} \left( 1 - 2 \frac{\mathbf{r} \otimes \mathbf{r}}{|\mathbf{r}|^2} \right) \mathbf{n}. \quad (\text{A.15})$$

- Navier: Linear elasticity for isotropic material with shear modulus  $\mu$  and Poisson ratio  $\nu$ ,

$$\mu \Delta \mathbf{u} + \frac{\mu}{1-2\nu} \nabla \nabla \cdot \mathbf{u} = 0, \quad (\text{A.16})$$

$$S(\mathbf{x}, \mathbf{y}) = -\frac{3-4\nu}{8\pi(1-\nu)} \log |\mathbf{r}| + \frac{1}{8\pi(1-\nu)} \frac{\mathbf{r} \otimes \mathbf{r}}{|\mathbf{r}|^2}, \quad (\text{A.17})$$

$$D(\mathbf{x}, \mathbf{y}) = \frac{1-2\nu}{4\pi(1-\nu)} \left( \frac{\mathbf{r} \cdot \mathbf{n} + \mathbf{n} \otimes \mathbf{r} - \mathbf{r} \otimes \mathbf{n}}{|\mathbf{r}|^2} + \frac{2}{1-2\nu} \frac{\mathbf{r} \cdot \mathbf{n} \mathbf{r} \otimes \mathbf{r}}{|\mathbf{r}|^4} \right). \quad (\text{A.18})$$

## References

1. Alpert, B.K.: Hybrid Gauss-trapezoidal quadrature rules. *SIAM J. Sci. Comput.* **20**, 1551–1584 (1999)
2. Atkinson, K.: The numerical solution of integral equations of the second kind. Cambridge University Press (1997)
3. Barnett, A.H.: Evaluation of layer potentials close to the boundary for Laplace and Helmholtz problems on analytic planar domains. *SIAM J. Sci. Comput.* **36**(2), A427–A451 (2014)
4. Barnett, A.H., Betcke, T.: Stability and convergence of the Method of Fundamental Solutions for Helmholtz problems on analytic domains. *J. Comput. Phys.* **227**(14), 7003–7026 (2008)
5. Barnett, A.H., Wu, B., Veerapaneni, S.: Spectrally-accurate quadratures for evaluation of layer potentials close to the boundary for the 2D Stokes and Laplace equations. *SIAM J. Sci. Comput.* (2014)
6. Beale, J., Lai, M.C.: A method for computing nearly singular integrals. *SIAM J. Numer. Anal.* **38**, 1902–1925 (2001)
7. Beale, J.T., Ying, W., Wilson, J.R.: A Simple Method for Computing Singular or Nearly Singular Integrals on Closed Surfaces. *Commun. Comput. Phys.* pp. 1–21 (2015)
8. Bogomolny, A.: Fundamental solutions method for elliptic boundary value problems. *SIAM J. Numer. Anal.* **22**(4), 644–669 (1985)
9. Bremer, J.: On the Nyström discretization of integral equations on planar curves with corners. *Applied and Computational Harmonic Analysis* **32**(1), 45–64 (2012)
10. Bremer, J., Gimbutas, Z.: A Nyström method for weakly singular integral operators on surfaces. *J. Comput. Phys.* **231**, 4885–4903 (2012)
11. Bremer, J., Rokhlin, V.: Efficient discretization of Laplace boundary integral equations on polygonal domains. *J. Comput. Phys.* **229**, 2507–2525 (2010)
12. Bremer, J., Rokhlin, V., Sammis, I.: Universal quadratures for boundary integral equations on two-dimensional domains with corners. *J. Comput. Phys.* **229**(22), 8259–8280 (2010)
13. Bruno, O.P., Knyansky, L.A.: A fast, high-order algorithm for the solution of surface scattering problems: basic implementation, tests, and applications. *J. Comput. Phys.* **169**, 80–110 (2001)
14. Colton, D., Kress, R.: Inverse acoustic and electromagnetic scattering theory, *Applied Mathematical Sciences*, vol. 93, second edn. Springer-Verlag, Berlin (1998)
15. Corona, E., Rahimian, A., Zorin, D.: A tensor-train accelerated solver for integral equations in complex geometries (2015)
16. Davis, P.J., Rabinowitz, P.: Methods of Numerical Integration. Academic Press, San Diego (1984)
17. Duffy, M.G.: Quadrature over a pyramid or cube of integrands with a singularity at a vertex. *SIAM journal on Numerical Analysis* **19**(6), 1260–1262 (1982)
18. Epstein, C.L., Greengard, L., Klöckner, A.: On the convergence of local expansions of layer potentials. *SIAM J. Numer. Anal.* **51**, 2660–2679 (2013)
19. Farina, L.: Evaluation of single layer potentials over curved surfaces. *SIAM Journal on Scientific Computing* **23**(1), 81–91 (2001)
20. Ganesh, M., Graham, I.: A high-order algorithm for obstacle scattering in three dimensions. *Journal of Computational Physics* **198**(1), 211–242 (2004)
21. Graglia, R.D., Lombardi, G.: Machine precision evaluation of singular and nearly singular potential integrals by use of gauss quadrature formulas for rational functions. *Antennas and Propagation, IEEE Transactions on* **56**(4), 981–998 (2008)
22. Graham, I., Sloan, I.: Fully discrete spectral boundary integral methods for Helmholtz problems on smooth closed surfaces in  $\mathbb{R}^3$ . *Numerische Mathematik* **92**(2), 289–323 (2002)
23. Hackbusch, W., Sauter, S.A.: On numerical cubatures of nearly singular surface integrals arising in bem collocation. *Computing* **52**(2), 139–159 (1994)
24. Hao, S., Barnett, A.H., Martinsson, P.G., Young, P.: High-order accurate Nyström discretization of integral equations with weakly singular kernels on smooth curves in the plane. *Adv. Comput. Math.* **40**(1), 245–272 (2014)
25. Helsing, J.: Integral equation methods for elliptic problems with boundary conditions of mixed type. *J. Comput. Phys.* **228**, 8892–8907 (2009)
26. Helsing, J.: Solving integral equations on piecewise smooth boundaries using the RCIP method: a tutorial (2012). Preprint, 34 pages, [arXiv:1207.6737v3](https://arxiv.org/abs/1207.6737v3)
27. Helsing, J., Ojala, R.: On the evaluation of layer potentials close to their sources. *J. Comput. Phys.* **227**, 2899–2921 (2008)
28. Hsiao, G., Wendland, W.L.: Boundary Integral Equations. *Applied Mathematical Sciences*, Vol. 164. Springer (2008)
29. Järvenpää, S., Taskinen, M., Ylä-Ojala, P.: Singularity extraction technique for integral equation methods with higher order basis functions on plane triangles and tetrahedra. *International journal for numerical methods in engineering* **58**(8), 1149–1165 (2003)
30. Johnson, C.G., Scott, L.R.: An analysis of quadrature errors in second-kind boundary integral methods. *SIAM Journal on Numerical Analysis* **26**(6), 1356–1382 (1989)
31. Kapur, S., Rokhlin, V.: High-order corrected trapezoidal quadrature rules for singular functions. *SIAM J. Numer. Anal.* **34**, 1331–1356 (1997)
32. Katsurada, M.: A mathematical study of the charge simulation method. II. *J. Fac. Sci. Univ. Tokyo Sect. IA Math.* **36**(1), 135–162 (1989)
33. Khayat, M.A., Wilton, D.R.: Numerical evaluation of singular and near-singular potential integrals. *Antennas and Propagation, IEEE Transactions on* **53**(10), 3180–3190 (2005)
34. Klöckner, A., Barnett, A.H., Greengard, L., O’Neil, M.: Quadrature by expansion: a new method for the evaluation of layer potentials. *J. Comput. Phys.* **252**(1), 332–349 (2013)

35. Kolm, P., Rokhlin, V.: Numerical quadratures for singular and hypersingular integrals. *Computers & Mathematics with Applications* **41**(3), 327–352 (2001)
36. Kress, R.: Boundary integral equations in time-harmonic acoustic scattering. *Mathl. Comput. Modelling* **15**, 229–243 (1991)
37. Kress, R.: On the numerical solution of a hypersingular integral equation in scattering theory. *J. Comput. Appl. Math.* **61**, 345–360 (1995)
38. Kress, R.: *Linear Integral Equations*, *Appl. Math. Sci.*, vol. 82, second edn. Springer (1999)
39. Lowengrub, J., Shelley, M., Merriman, B.: High-order and efficient methods for the vorticity formulation of the euler equations. *SIAM Journal on Scientific Computing* **14**(5), 1107–1142 (1993)
40. Nachtigal, N.M., Reddy, S.C., Trefethen, L.N.: How Fast are Nonsymmetric Matrix Iterations? *SIAM Journal on Matrix Analysis and Applications* **13**(3), 778–795 (1992)
41. Ojala, R., Tornberg, A.K.: An accurate integral equation method for simulating multi-phase Stokes flow. *J. Comput. Phys.* **298**, 145–160 (2015)
42. Pozrikidis, C.: *Boundary Integral and Singularity Methods for Linearized Viscous Flow*. Cambridge Tests in Applied Mathematics. Cambridge University Press (1992)
43. Quaife, B., Biros, G.: High-volume fraction simulations of two-dimensional vesicle suspensions. *J. Comput. Phys.* **274**, 245–267 (2014)
44. Rachh, M., Klöckner, A., O’Neil, M.: Fast algorithms for quadrature by expansion I: Globally valid expansions. arXiv preprint arXiv:1602.05301 (2016)
45. Rahimian, A., Lashuk, I., Veerapaneni, S.K., Chandramowlishwaran, A., Malhotra, D., Moon, L., Sampath, R., Shringarpure, A., Vetter, J., Vuduc, R., Zorin, D., Biros, G.: Petascale Direct Numerical Simulation of Blood Flow on 200K Cores and Heterogeneous Architectures. In: 2010 ACM/IEEE International Conference for High Performance Computing, Networking, Storage and Analysis, November, pp. 1–11. IEEE (2010)
46. Schwab, C., Wendland, W.L.: On numerical cubatures of singular surface integrals in boundary element methods. *Numerische Mathematik* **62**(1), 343–369 (1992)
47. Sidi, A., Israeli, M.: Quadrature methods for periodic singular and weakly singular fredholm integral equations. *Journal of Scientific Computing* **3**(2), 201–231 (1988)
48. Strain, J.: Locally corrected multidimensional quadrature rules for singular functions. *SIAM Journal on Scientific Computing* **16**(4), 992–1017 (1995)
49. Tlupova, S., Beale, J.T.: Nearly singular integrals in 3d Stokes flow. *Commun. Comput. Phys.* **14**(5), 1207–1227 (2013)
50. Tornberg, A.K., Shelley, M.J.: Simulating the dynamics and interactions of flexible fibers in Stokes flows. *Journal of Computational Physics* **196**(1), 8–40 (2004)
51. Trefethen, L.N., Bau III, D.: *Numerical Linear Algebra*. SIAM (1997)
52. Veerapaneni, S.K., Rahimian, A., Biros, G., Zorin, D.: A fast algorithm for simulating vesicle flows in three dimensions. *Journal of Computational Physics* **230**(14), 5610–5634 (2011)
53. Yarvin, N., Rokhlin, V.: Generalized gaussian quadratures and singular value decompositions of integral operators. *SIAM Journal on Scientific Computing* **20**(2), 699–718 (1998)
54. Ying, L., Biros, G., Zorin, D.: A high-order 3D boundary integral equation solver for elliptic PDEs in smooth domains. *J. Comput. Phys.* **216**, 247–275 (2006)
55. Ying, W., Beale, J.T.: A fast accurate boundary integral method for potentials on closely packed cells. *Commun. Comput. Phys.* **14**, 1073–1093 (2013)